Supporting Information

Sha et al. 10.1073/pnas.1501137112

SI Text

Paleogeographic Reconstruction. The illustration of Pangea in Fig. 1 and Fig. S1 was redrafted from a reconstruction for the Triassic–Jurassic transition (201.6 Ma) produced by the PALEOMAP Project (1–3) displayed using GoogleEarth. The positions of the Pucara (Peru), Newark–Hartford (United States), Bristol Channel (United Kingdom), and Junggar (Western China) basins on Pangea were then translated as rigid plate south about 3° along the prime meridian to bring their paleolatitude into agreement with ref. 4. This slight reconfiguration produced virtually no change in the latitude of the Junggar Basin at about 60° N from the PALEOMAP reconstruction.

A 60° paleolatitude for the Junggar is in agreement with several additional lines of evidence. Paleomagnetic determinations of paleolatitude of Triassic–Jurassic strata from Junggar and the adjacent Tarim Basin (e.g., ref. 5), although scarce and wholly from sedimentary rocks, suggest a paleolatitude close to that of the present 45° N. The existing paleomagnetic literature, however, does not take into account the effects of compaction-induced inclination error (4, 6, 7), which is greatest at the latitudes suggested by Carroll et al. (8) for the Junggar Basin. Correcting for paleomagnetic inclination error has proved crucial in reconciling discrepant igneous and sedimentary paleomagnetic data in Eastern North America and Greenland (6) in strata correlative to those discussed here, and a approximate correction of 10–15° of paleolatitude is plausible for the Junggar Basin, an estimate of which can be tested by the collection of additional paleomagnetic data. Carroll et al. (8) show similarly high latitude for the basin (~60° N) based on the plate-tectonic context. The estimated position of 60° N as shown in the PALEOMAP reconstructions is therefore plausibly the best available estimate of latitude (Fig. 1).

Location of the Haojiagou Section. The Haojiagou and Badaowan formations outcrop more or less continuously in badlands along the Haojiagou (gou = valley) located at about 50 km southwest of Ürümqi City on the southern margin of the Junggar Basin of the northern Xinjiang Uygur (Uighur) Autonomous Region, Northwestern China (Figs. 1 and 2 and Figs. S1 and S2). About 1,100 m of this section is the basis of this report, beginning at ~43° 38.452' N, 87° 13.266' E and ending 43° 39.889' N, 87° 12.170' E. The section has been studied in various aspects (e.g., refs. 9–16), but only one summary on the cyclostratigraphy has been published to date (17). The data presented here were collected on the east side of the valley.

Construction of the LITH Index. The Haojiagou section was described by Deng et al. (18), with the lithologic data being collected and obtained during fieldwork in 1996, 1998, and 2008. The initial analysis is distinguished by the thickness and lithologic features, reflecting the paleoenvironment, of each measured layer. By using the semiquantitative classification of lithology called the "LITH" index (19), a hierarchy of cycles based on sedimentary rock types was recognized, and the different digital numbers (LITH values) were defined for various rock types (Table 1). The variations (values between 10 and 130) in LITH produce the obvious cyclicity. We converted two measurements (depth measurements and LITH measurement), by interpolating a LITH value at 0.1-m intervals within each layer, into a numerical time series forming a new time series, LITH time series, on which our times series analyses were performed (Fig. S3).

Temporal Constraints on the Junggar Latest Triassic and Earliest Jurassic Strata. Forty samples spanning the boundary of the Haojiagou and Badaowan formations, Junggar Basin, China were examined for palynology. Of these samples, 35 were usefully productive samples (Fig. S3) and formed the basis of the range chart shown in Fig. 3. Our analysis focuses on the ETE, supercedes the palynological analysis in Sha et al. (15), and includes more samples for higher resolution. Samples were processed at Global GeoLab Ltd., Canada (www.globalgeolab.com) following standard methods. The palynological slides and residues are stored at the Department of Palaeobiology, Swedish Museum of Natural History.

The sedimentary successions of the Haojiagou and Badaowan formations at the Haojiagou section yielded well-preserved miospore assemblages of medium diversity; 60 species of fossil pollen and spore taxa were identified in this study, together with a putative dinoflagellate (*Chytroeisphaeridia* sp.) and the chlorophyte (green alga) *Botryococcus braunii*. The age assessment is based on a combination of last and first appearance datums for key taxa (Fig. S3). Typical Triassic elements persist up to bed 52, including *Lunatisporites rhaeticus* and *Limbosporites* spp., whereas the abundant occurrence of *Retritriletes semimuris* and *Retritriletes austroclavatidites* in bed 53 suggests a Hettangian age (20), and the end of the ETE interval (Fig. 3 and Fig. S3).

The presence of *Cerebropollenites macroverrucosus* and *Callialasporites trilobatus* in bed 81 suggests a Sinemurian–Pliensbachian age (21) for that level. The comparison with European and Australian palynostratigraphical schemes is tentative because these regions represent different floral paleo-provinces from those previously described for this region (9, 12) and because correlative zonation schemes between the regions have not been erected. Identification of the Hettangian–Sinemurian boundary to the Haojiagou section is more problematic because there is apparently no change in sporomorph composition across that boundary at the base-Sinemurian GSSP in the United Kingdom or Europe in general (22–24).

Thus, based on the palynology, we have placed the top of the extinction interval, still in the late Rhaetian, at the last appearance datum (LAD) of the taeniate gymnosperm pollen *L. rhaeticus*. This sporomorph is regarded as a near-end-Rhaetian marker in Europe (including the United Kingdom), Greenland, and Eastern North America (25–29), where its last appearance occurs close to and above the initial expression of the end-Triassic extinction. In Eastern North America, the last appearance of this pollen taxon occurs in strata about 60 ky younger than the initiation of the initial ETE, as constrained by both U-Pb dates and astrochronology (30), and the Triassic–Jurassic boundary occurs about 40 ky after that based on extraopolation and correlation with United Kingdom sections (31). Thus, we use the LAD of *L. rhaeticus* as a tie point to pin the ETE within the studied successions (Figs. 2 and 3).

In terms of floral provinces, Sun et al. (ref. 13 and references therein) argue that the Haojiagou (Late Triassic) floral assemblage belongs to the *Danaeopsis–Symopteris* assemblages [updated from the original *Danaeopsis–Bernoullia* assemblage because the latter name has a prior synonym that is a malvaceous angiosperm (Bombacaceae)] (32), "Northern China" continental floristic province whereas the Badaowan (Early Jurassic) florules belong to the *Coniopters–Phoenicopsis* or "Siberian" continental floristic province, both of which are typical northern-hemisphere, high-latitude humid assemblages. The transition between the *Danaeopsis–Symopteris* and *Coniopters–Phoenicopsis* assemblages around the Triassic–Jurassic transition is interpreted as indicating a transition to more humid and warm conditions (13). Generally, warm and humid conditions in both formations are consistent with the broad-leaf gymnosperm assemblage and the presence of common coal and are consistent with many sedimentary basins in the early Mesozoic northern-hemisphere high latitudes (33, 34) although they clearly represent nonanalog communities and although it is very difficult to assess whether these assemblages have any time significance.

In contrast, the numerical ages of the ETE are now well-understood at 201.564 ± 0.015 Ma (30), the Triassic–Jurassic boundary between 201.32 ± 0.13 Ma and 201.39 ± 0.14 Ma (35) [mean of 201.36 ± 0.14 Ma, rms error], and the Hettangian –Sinemurian boundary at about 199.46 ± 0.17 Ma (corrected from the original 199.43 ± 0.10 Ma date of ref. 36), based on zircon $^{206}Pb/^{238}U$ ages and astrochronology, with varying degrees of precision and additional uncertainty (up to 0.1%) due to very slightly different interlaboratory methods. The duration of the Hettangian is thus now well-established, with the most recent estimates being 2 My (U-Pb; ref. 37), 1.8 My (astrochronology; refs. 31, 38, and 39), and 1.88 ± 0.16 My (U-Pb; refs. 30 and 36). These durations are all close to the duration of 2 My for the Hettangian in the most recent timescale compilation (40). Based on the U-Pb dates and astrochronology in ref. 30, we used the last appearance of *L. rhaeticus* to tie the Badaowan section at 201.50 ± 0.1 Ma (Figs. 2 and 3 and Fig. S3).

Analytical Methods. The FFT and MTM spectra (Fig. 4 and Figs. S4 and S5) were developed using Analyseries (2.0) (41), and the evolutive wavelet spectrum was computed using the Matlab script of Torrence and Compo (42) (paos.colorado.edu/research/wavelets/). For all data, the original depth series was interpolated with an increment of 0.1 m. Data were divided into two series: a low LITH index series with values from 20 to 60, which were then reversed and rescaled to range from 0 to 40 (with 40 being fine grained and 0 being coarse), and a high LITH index series with values from 60 to 140 (with 60 being fine grained and 140 being coarse). For the MTM spectra the following Analyseries options were used: linear trend was removed, medium confidence vs. resolution was selected, width.ndata product was 4, six windows were used, output was resampled from 0 to 2 with a step of 0.001, and inferior and superior error bars and amplitude spectra were computed (for Fig. 4 and Fig. S4). For the FFT, periodograms (power spectra) were prepared with the following Analyseries options: linear trend was removed, Bartlett window was used, and output was resampled from 0 to 2 with a step of 0.001. Note that Analyseries does not use adaptive weighting and thus tends to overestimate the number of significant harmonics in frequencies with low power. Consequently, we regarded only cycles with high power and high f-test statistics as having been meaningful. For the 405-ky filtered clipped-LITH data, a frequency of 0.0289855 m per cycle was used with a bandwidth of 0.005, with a Gaussian shape. For the 405-ky frequency of the total organic carbon (TOC) data of ref. 38, a frequency of 0.00062486 cm per cycle was used with a bandwidth of 0.0003 and a Gaussian shape. The modulation of obliquity (Fig. S7) is based on bandpass filtering the clipped LITH series with a 0.275 m per cycle frequency and a bandwidth of 0.02 and a Gaussian shape, which was then demodulated [amplitude modulated (AM) filtered]. The result was compared with a bandpass filtering of the clipped LITH series at a frequency of 0.0142857 m per cycle and a bandwidth of 0.01 and a Gaussian shape. The wavelet spectra were computed using the Matlab script of Torrence and Compo (42) (paos.colorado.edu/research/wavelets/software.html) with dt = 0.1 and all other options at the default values.

1. Paleomap Project. Available at www.globalgeology.com/. Accessed February 26, 2015.
2. Scotese CR, Moore TL, Dreher CT (2013) Teaching and research tools for deep time studies: Ancient Earth app, Global Geology website, and the PALEOMAP PaleoAtlas for ArcGIS. *GSA Abstracts with Programs* 45:233.
3. Scotese CR (2013) *PALEOMAP PaleoAtlas for ArcGIS, Jurassic & Triassic* (PALEOMAP Project, Evanston, IL), Vol 3.
4. Kent DV, Tauxe L (2005) Corrected Late Triassic latitudes for continents adjacent to the North Atlantic. *Science* 307(5707):240–244.
5. Choulet F, et al. (2013) First Triassic palaeomagnetic constraints from Junggar (NW China) and their implications for the Mesozoic tectonics in Central Asia. *J Asian Earth Sci* 78:371–394.
6. Tauxe L (2005) Inclination flattening and the geocentric axial dipole hypothesis. *Earth Planet Sci Lett* 233:27–261.
7. Tauxe L, Kodama KP, Kent DV (2008) Testing corrections for paleomagnetic inclination error in sedimentary rocks: A comparative approach. *Phys Earth Planet Inter* 169:152–165.
8. Carroll AR, Graham SA, Smith ME (2010) Walled sedimentary basins of China. *Basin Res* 22(1):17–32.
9. Ashraf AR, et al. (1999) The Triassic-Jurassic boundary in the Junggar Basin (NW China): Preliminary palynostratigraphic results. *Acta Palaeobotanica* 1999(Suppl 2):85–91.
10. Ashraf AR, Wang X, Sun G, Li J, Mosbrugger V (2001) Palynostratigraphic analysis of the Huangshanjie-, Haojiagou- and Badaowan formations in the Junggar Basin (NW China). *Proceedings of the Sino-German Cooperation Symposium on Paleontology, Geological Evolution and Environmental Changes of Xinjiang, China* (Jilin University, Ürümqui, China), pp 40–64.
11. Ashraf AR, Sun Y-W, Li J, Sun G, Mosbrugger V (2004) Palynostratigraphic analysis of the Huangshanjie-, Haojiagou-, Badaowan-, Sangonghe- and Xishanyao Formation (Upper Triassic-Middle Jurassic) in the Southern Junggar Basin (NW China). *Proceedings of the Sino–German Cooperation Symposium on Paleontology, Geological Evolution and Environmental Changes of Xinjiang, China, Ürümqi*, eds Sun G, Mosbrugger V, Ashraf AR, Sun YW (Jilin University, Ürümqui, China), pp 41–44.
12. Ashraf AR, et al. (2010) Triassic and Jurassic palaeoclimate development in the Junggar Basin, Xinjiang, northwest China: A review and additional lithological data. *Palaeobiodivers Palaeoenviron* 90(3):187–201.
13. Sun G, Mosbrugger V, Miao Y-Y, Ashraf AR (2010) The Upper Triassic to Middle Jurassic strata and floras of the Junggar Basin, Xinjiang, Northwest China. *Palaeobiol Palaeoenviron* 90(3):203–214.
14. Hornung J, Hinderer M (2011) Depositional dynamics and preservation potential in a progradational lacustrine fluvio-deltaic setting: Implications for high-resolution sequence stratigraphy (Upper Triassic, Northwestern China). *From River to Rock Record: The Preservation of Fluvial Sediments and Their Subsequent Interpretation*, eds Davidson SK, Leleu S North CP (SEPM Society for Sedimentary Geology, Tulsa, OK), SEPM Special Publication No. 97, pp. 281–310.
15. Sha J, et al. (2011) The stratigraphy of the Triassic-Jurassic boundary successions of the southern margin of Junggar Basin, northwestern China. *Acta Geol Sin* 85(2): 421–436.
16. Sha J, et al. (2012) *Type-Boundary Section of Non-Marine Base-Jurassic and Regional Correlation: Research Report Establishing Stages of Major Dates in China*, ed The Third National Stratigraphical Committee of China (Geological Publishing House, Beijing), pp 148–159. In Chinese.
17. Sha J, et al. (2010) Astronomical calibrated time intervals for the non-marine Badaowan Formation, Lower Jurassic in Haojiagou of Ürümqi City, Western China. *Earth Sci Front* 17(Special Issue):22–23.
18. Deng S, et al. (2010) *The Jurassic System of Northern Xinjiang, China* (University of Science and Technology of China Press, Heifei, China).
19. Xu D, Ji X, Ceng X, Luo Z (2000) Study of high resolution continental cyclostratigraphy: Example of Badaowan Formation in Haojiagou, Xinjiang. *Proceedings of the Third National Stratigraphical Conference of China* (Geological Publishing House, Beijing), pp. 191–196. In Chinese.
20. Vajda V, Bercovici A (2014) The global vegetation pattern across the Cretaceous–Paleogene mass extinction interval: A template for other extinction events. *Global Planet Change* 122:29–49.
21. Bomfleur B, McLoughlin S, Vajda V (2014) Fossilized nuclei and chromosomes reveal 180 million years of genomic stasis in royal ferns. *Science* 343(6177):1376–1377.
22. Weiss M (1989) Die Sporenfloren aus Rät und Jura Südwest-Deutschlands und ihre Beziehung zur Ammoniten-Stratigraphie. *Palaeontographica B* 215:1–168.
23. Page KN, et al. (2000) East Quantoxhead, Somerset: A candidate global stratotype section and point for the base of the Sinemurian Stage (Lower Jurassic). *GeoResearch Forum* 6:163–171.
24. Bloos G, Page KN (2002) Global stratotype section and point for base of the Sinemurian Stage (Lower Jurassic). *Episodes* 25(1):22–28.
25. Kürschner WM, Herngreen GFW (2010) Triassic palynology of central and northwestern Europe: A review of palynofloral diversity patterns and biostratigraphic subdivisions. *Geol Soc Lond Spec Publ* 334:263–283.
26. Bonis NR, Kürschner WM (2012) Vegetation history, diversity patterns, and climate change across the Triassic/Jurassic boundary. *Paleobiology* 38(2):240–264.
27. Mander L, Kürschner WM, McElwain JC (2013) Palynostratigraphy and vegetation history of the Triassic–Jurassic transition in East Greenland. *J Geol Soc London* 170:37–46.
28. Cirilli S, et al. (2009) Latest Triassic onset of the Central Atlantic Magmatic Province (CAMP) volcanism in the Fundy Basin (Nova Scotia): New stratigraphic constraints. *Earth Planet Sci Lett* 286(3–4):514–525.
29. Bonis NR, Ruhl M, Kürschner WM (2010) Milankovitch-scale palynological turnover across the Triassic–Jurassic transition at St. Audrie's Bay, SW UK. *J Geol Soc London* 167:877–888.
30. Blackburn TJ, et al. (2013) Zircon U-Pb geochronology links the end-Triassic extinction with the Central Atlantic Magmatic Province. *Science* 340(6135):941–945.

31. Whiteside JH, Olsen PE, Eglinton T, Brookfield ME, Sambrotto RN (2010) Compound-specific carbon isotopes from Earth's largest flood basalt eruptions directly linked to the end-Triassic mass extinction. *Proc Natl Acad Sci USA* 107(15):6721–6725.
32. Kustatscher E, Pott C, van Konijnenburg-van Cittert JHA (2011) A contribution to the knowledge of the Triassic fern genus *Symopteris*. *Rev Palaeobot Palynol* 165(1):41–60.
33. Lu B, Deng S, Qi X (2000) Jurassic climatic events of North China and their geological significance. *GeoResearch Forum* 6:463–472.
34. Willis KJ, McElwain JC (2002) *The Evolution of Plants* (Oxford Univ Press, New York).
35. Wotzlaw J-F, et al. (2014) Towards accurate numerical calibration of the Late Triassic: High-precision U-Pb geochronology constraints on the duration of the Rhaetian. *Geology* 42:571–574.
36. Guex J, et al. (2012) Geochronological constraints on post-extinction recovery of the ammonoids and carbon cycle perturbations during the Early Jurassic. *Palaeogeogr Palaeoclimatol Palaeoecol* 346–347:1–11.
37. Schaltegger U, Guex J, Bartolini A, Schoene B, Ovtcharova M (2008) Precise U–Pb age constraints for end-Triassic mass extinction, its correlation to volcanism and Hettangian post-extinction recovery. *Earth Planet Sci Lett* 267:266–275.
38. Ruhl M, et al. (2010) Astronomical constraints on the duration of the early Jurassic Hettangian stage and recovery rates following the end-Triassic mass extinction (St. Audrie's Bay/East Quantoxhead, UK). *Earth Planet Sci Lett* 295:262–276.
39. Olsen PE, Kent DV, Whiteside JH (2011) Implications of the Newark Supergroup-based astrochronology and geomagnetic polarity time scale (Newark-APTS) for the tempo and mode of the early diversification of the Dinosauria. *Earth Environ Sci Trans R Soc Edinburgh* 101:201–229.
40. Gradstein FM Ogg JG, Schmitz M, Ogg G, eds (2012) *The Geologic Time Scale 2012* (Elsevier Science, Oxford).
41. Paillard D, Labeyrie L, Yiou P (1996) Macintosh program performs time-series analysis. *Eos Trans AGU* 77:379.
42. Torrence C, Compo GP (1998) A practical guide to wavelet analysis. *Bull Am Meteorol Soc* 79:61–78.
43. Maron M, et al. (2015) Magnetostratigraphy of the Pignola-Abriola section: new constraints for the Norian/Rhaetian boundary. *Geol Soc Am Bull*, 10.1130/B31106.

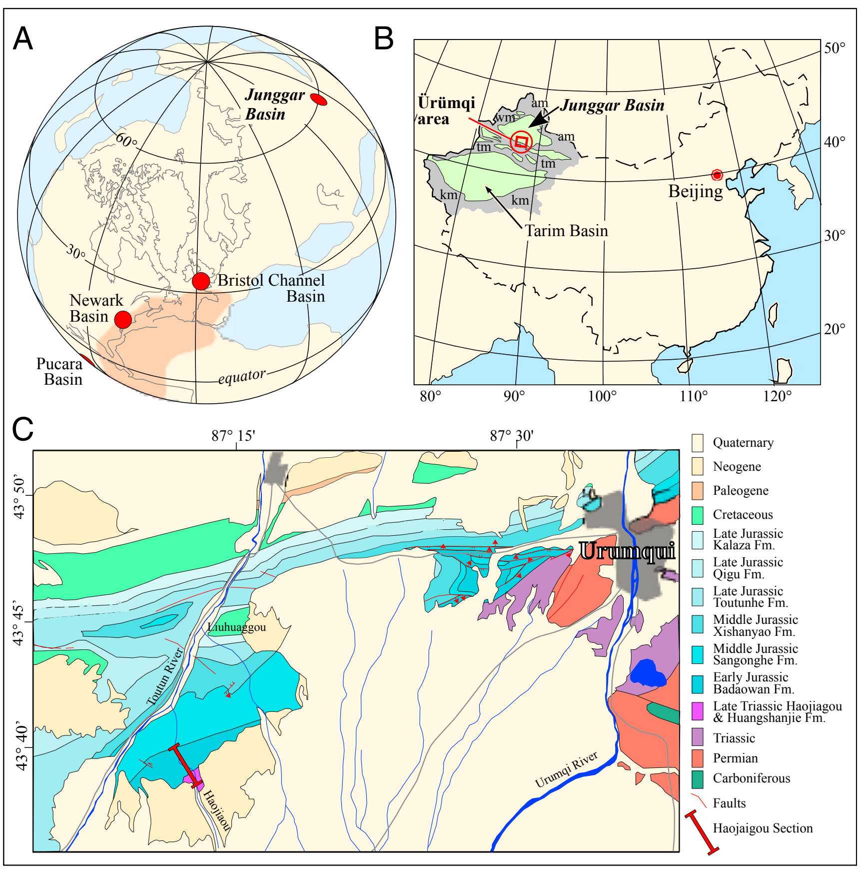

Fig. S1. Paleogeographic and present position of the Junggar Basin. (*A*) Paleogeographic position of the Junggar Basin, Bristol Channel, Newark–Hartford, and Pucara basins with the distribution of the Central Atlantic Magmatic Province shown in darker tan. (*B*) Map of the Junggar and Tarim basins, Northwest China (based on ref. 8). as, Altay Shan; ks, Kunlun Shan; ts, Tian Shan. (*C*) Map of the surficial geology of the Ürümqi area showing the position of the Haojiagou section.

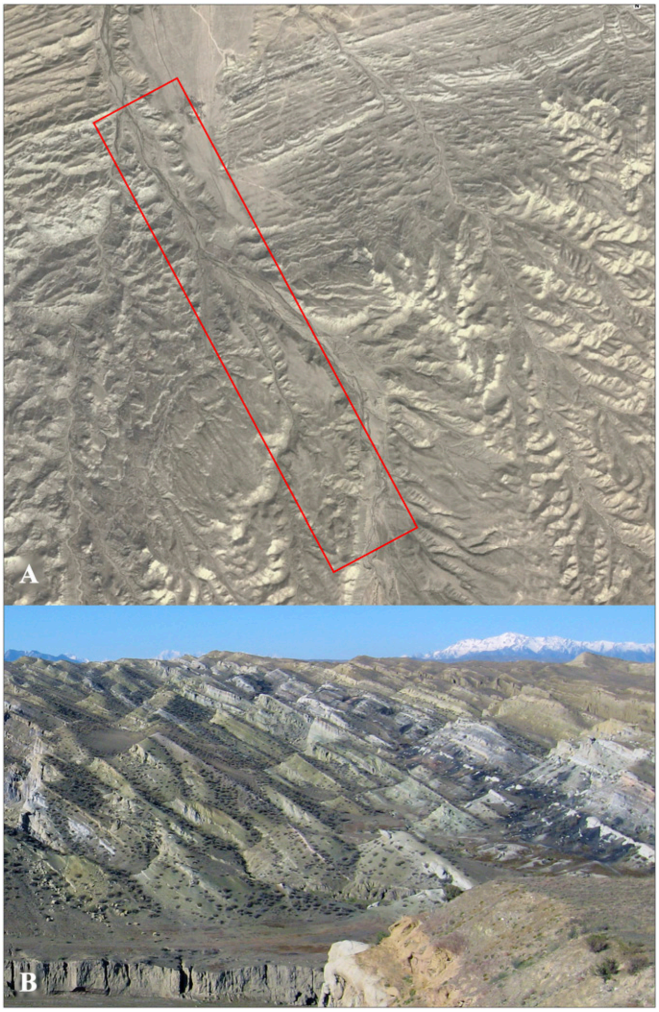

Fig. S2. Images of the Junggar Basin section. (*A*) GoogleEarth image of Haojiagou section (red box), the location of which is shown in Fig. S1, showing relatively undeformed strata tilting to the north-northeast. (*B*) Photograph of portion of the Haojiagou section including beds 45–53, looking west across the valley. The section was measured on the east side of Haojiagou from where the photograph was taken.

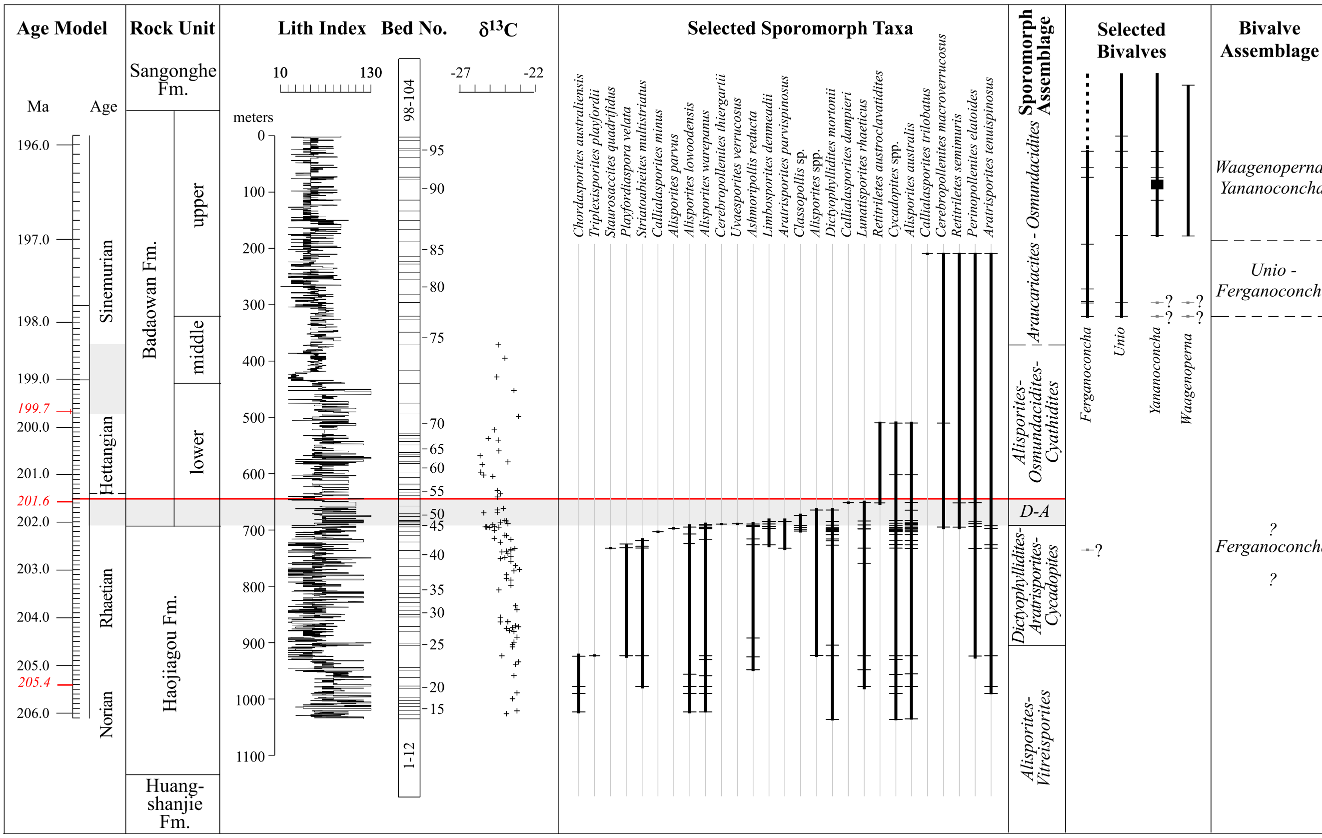

Fig. S3. Measured LITH index, simplified stratigraphic column, bed numbers, biostratigraphic data, and age model for the Haojiagou section. The occurrences of taxa are shown by ticks based on new counts, on which the new sporomorph assemblages are based. The red line marks the top of the range of *L. rhaeticus* in our studied section, the marker taxon used to correlate the lower Badaowan Formation to the eastern North American and United Kingdom sections (Fig. 4). The numerical ages in the age model are based on recognition of the 405-ky cycle in the MTM spectra, with the ages indicated in red representing the projections into the section of the initial end-Triassic extinction (201.6 Ma) and the Hettangian–Sinemurian boundary (199.7 Ma; thicker red bar indicated uncertainty from Fig. 4), and the Norian–Rheatian boundary date is based on the Newark–Hartford APTS (interpreted by ref. 43) and the independent $^{206}Pb/^{238}U$ zircon Pucara Basin ashes (35). Gray fill in the standard ages indicates the range of possible boundary picks internal to data from the Junggar Basin itself, and the dashed lines indicate stage boundaries as suggested in ref. 17. The $\delta^{13}C$ data are from ref. 33. All data are registered to the bed numbers as measured by this field party in the Haojiagou section.

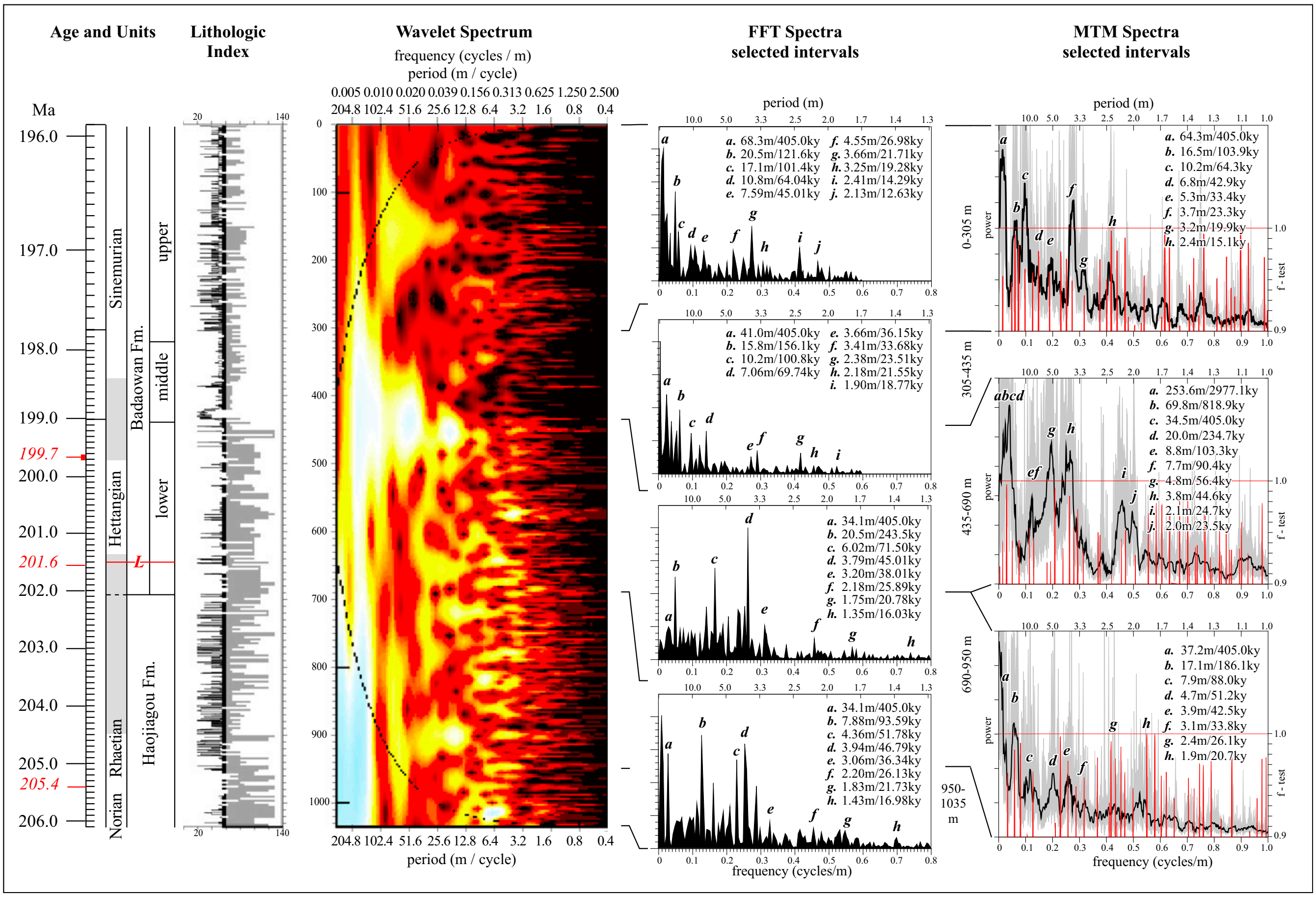

Fig. S4. Wavelet spectrum, FFT, and MTM spectral results from the clipped LITH scale (grayed part clipped off) of the upper part of the Haojiagou Formation through the upper member of the Badaowan Formation in the Haojiagou section. Conventions for temporal information are as in Fig. S3. In the evolutive FFT, white is the highest relative power and black is the lowest. In the FFT spectra, high-amplitude peaks are labeled with their periods in meters and ky (kiloyears) assuming recognition of the 405-ky cycle. In the MTM spectra, only those peaks in spectral power that have f-test significance above the 0.9 level and high amplitude are labeled, and they are labeled in meters and kiloyears based on recognition of the 405-ky level.

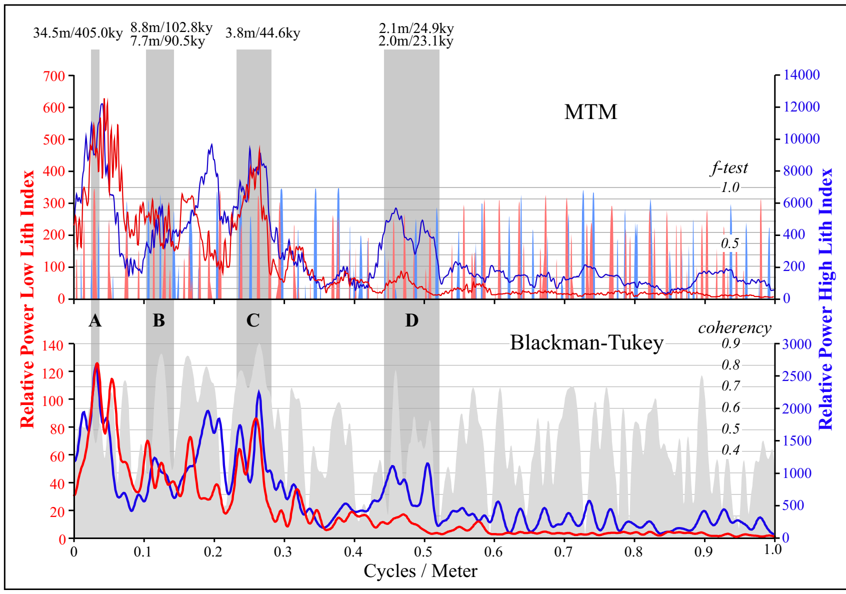

Fig. S5. Comparison of spectral analysis for the low LITH Index values (black in Figs. S3 and S4) and the high Index values (gray in Figs. S3 and S4) using the multitaper method (MTM) with the f-statistic and the Blackman–Tukey method with coherence for the interval 435–690 m. The bands corresponding to orbital frequencies are show in gray and are as follows: (*A*) 405-ky eccentricity (40.0–27.8 m) 469.6–326.4 ky; (*B*) ∼100-ky eccentricity (9.7–7.0m), 114.0–82.7 ky; (*C*) obliquity (4.3–3.6 m), 50.6–41.6 ky; and (*D*) climatic precession (2.3–1.9 m), 26.6–22.5 ky. They are also labeled with the major specific picks from Fig. S4. Note that the two methods give essentially the same results on the two sets of values from the LITH index, with the orbital period being highly significant (f > 0.9), high relative spectral power, and coherence (>0.6).

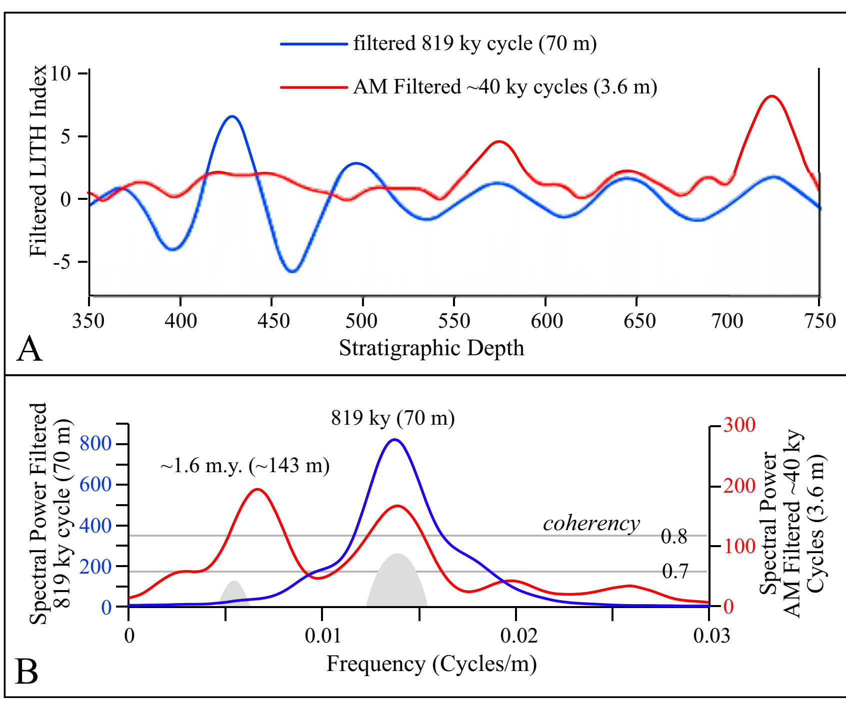

Fig. S6. Modulation of the lithological expression of ∼40-ky (3.6-m) obliquity cycle by the ∼819-ky (∼70-m) cycle identified by spectral analysis (Fig. S4). (*A*) Comparison of AM filtered (Hilbert transform) of the filtered ∼40-ky cycle from the clipped LITH series, with the filtered ∼819-ky (∼70-m) cycle from the clipped LITH series. Note the close correspondence between the two independent filtered series showing that the lithological expression of ∼40-ky (3.6-m) obliquity cycle is in fact modulated by the ∼819-ky (∼70-m) cycle. (*B*) Blackman–Tukey spectra and coherence of the two series in *A*, showing quantitatively that the lithological expression of ∼40-ky (3.6-m) obliquity cycle is coherent (above 0.7) with the filtered ∼819-ky (∼70-m) cycle. Note that some modulation by the 2 × 819-ky cycle is expected within the obliquity band. The clipped LITH index series was bandpass filtered by frequency of 0.275 cycles/m (3.6-m period) with a bandwidth of 0.02 and a Gaussian shape. The resulting series was AM filtered (Hilbert transform). The same clipped LITH index series was bandpass filtered at a frequency of 0.014285 cycles/m (70-m period) with a bandwidth of 0.005 and Gaussian shape. Blackman–Tukey spectra were obtained with Analyseries using a Bartlett window, with a bandwidth of 0.00416551, and the nonzero coherence is higher than 0.6056.

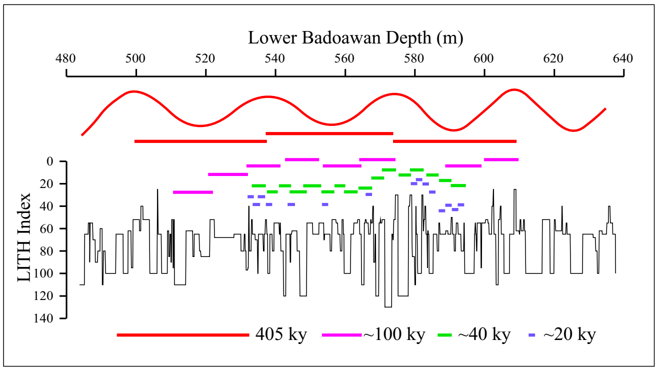

Fig. S7. The various major cycles discussed in this paper as they appear in the LITH index.

Table S1. LITH index values (rock colors range from black to light gray)

Lithology	Environment	LITH value
Coal or coal seam	Dysoxic sediment-starved lake or swamp	10
Shale, carbonaceous shale	Dysoxic lake	25
Mudstone	Shallow lake	30
Silty mudstone	Shallow lake	40
Muddy siltstone	Shallow lake or paleosol	50
Fine-grained siltstone	Shallow lake or paleosol	55
Medium-grained siltstone	Floodplain or paleosol	60
Coarse-grained siltstone	Floodplain or paleosol	65
Fine-grained sandstone	Floodplain and fluvial	70
Fine-grained sandstone	Fluvial	80
Medium-grained sandstone	Fluvial	90
Coarse-grained sandstone	Fluvial	100
Fine conglomerate: ≤4-cm clasts	Fluvial	110
Medium conglomerate: ≤8-cm clasts	Fluvial	120
Coarse conglomerate: >8-cm clasts	Fluvial	130

Table S2. U-Pb and astrochronological ages compared: Explanation

Horizon or unit	Newark igneous U-Pb	Newark–Hartford APTS	Pucara Basin U-Pb	Bristol Channel Basin Pucara*/Newark†
Hettangian–Sinemurian boundary	Not applicable	199.70 ± 0.02	199.46 ± 0.17‡	199.61/199.66
Hook Mountain Basalt	200.916 ± 0.064§	200.93 ± 0.02	Not applicable	Not applicable
Preakness Basalt	201.274 ± 0.032¶	201.28 ± 0.02	Not applicable	Not applicable
Rhaetian–Hettangian boundary	Not applicable	201.42 ± 0.02	201.36 ± 0.14#	201.32/201.37
Orange Mountain Basalt	201.520 ± 0.034‖	201.52 ± 0.02**	Not applicable	Not applicable
End–Triassic extinction	201.564 ± 0.015††	201.56 ± 0.02‡‡	201.51 ± 0.15	201.51/201.56

*Using the Pucara ash-based ETE as a tie point (35).
†Using the Newark igneous-based ETE as a tie point (30).
‡Zircon $^{206}Pb/^{238}U$ age of Pucara Basin ash LM4-19B at the Hettangian–Sinemurian boundary, originally published as 199.43 ± 0.1 Ma (15) but adjusted here to 199.46 ± 0.17 based on a regression of ages of ashes dated by both Guex et al. (36) and Wotzlaw et al. (35), the latter using updated EARTHTIME protocols (www.earth-time.org). B. Schoene (pers. comm., 02/15) has recalculated this age using current EarthTime protocols as 199.51 ± 0.10.
§Zircon $^{206}Pb/^{238}U$ age of the Butner Diabase that applies to the Hook Mountain Basalt (30).
¶Zircon $^{206}Pb/^{238}U$ age of flow 2 of the Preakness Basalt (30).
#Average age and rms error of marine Pucara Basin ashes LM4-100/101 and LM4-90 zircon $^{206}Pb/^{238}U$ ages that bracket the ammonite-calibrated Triassic–Jurassic boundary (35).
‖Zircon $^{206}Pb/^{238}U$ age of the Palisade Sill that applies to the Orange Mountain Basalt (30).
**Age of the Triassic–Jurassic boundary as projected into the Newark APTS (31).
††Age of the continental ETE in the basins of Eastern North America and Morocco derived from zircon $^{206}Pb/^{238}U$ dates and astrochronology (30).
‡‡Rounded age of the continental ETE (30) used as a tie point for the Newark astrochronology.